

Doubly resonant $\chi^{(2)}$ nonlinear photonic crystal cavity based on a bound state in the continuum: supplementary material

MOMCHIL MINKOV^{1, 3}, DARIO GERACE², AND SHANHUI FAN^{1,*}

¹Department of Electrical Engineering, Stanford University, Stanford, CA 94305, USA

²Dipartimento di Fisica, Università di Pavia, via Bassi 6, 27100 Pavia, Italy

³e-mail: mminkov@stanford.edu

*Corresponding author: shanhui@stanford.edu

Published 8 August 2019

This document provides supplementary information to "Doubly resonant $\chi^{(2)}$ nonlinear photonic crystal cavity based on a bound state in the continuum," <https://doi.org/10.1364/OPTICA.6.001039>. We provide details regarding the simulations discussed in the paper, and show larger images of the cavity modes. We also discuss some of the details relating to Eqs. (2) and (4) in the main text. Finally, we demonstrate that resonance tuning of the cavity modes into the doubly resonant condition is possible using either one of the photonic crystal structural parameters.

SIMULATIONS

The heterostructure cavity modes presented in the paper were computed using Lumerical FDTD Solutions. The full three-dimensional simulation domain for the cavity of Fig. 2(b)-(d) in the main text is schematically shown in Fig. S1. Outside of the outer PhC region, there is a region of un-patterned slab. Absorbing perfectly-matched layer (PML) boundary conditions were applied on all sides outside of this simulation domain. We used a source close to the center of the heterostructure to excite the resonant modes.

NEAR AND FAR FIELDS

In Figs. S2(a), S3(a), and S4(a), we plot an enlarged version of the field profiles shown in Fig. 2(b)-(d) in the main text, respectively. In panels (b) of these three Figures, we also show a cross-section view of the field in the xz -plane at $y = 0$. Finally, in Fig. S5, we plot the far-field profiles for all three modes and for a range of values of the core region size.

NONLINEAR OVERLAP

We study the nonlinear overlap integral between two heterostructure modes $E_{1,p}(\mathbf{r})$, $E_{2,p'}(\mathbf{r})$ that can be written as

$$\mathbf{E}_{i,p}(\mathbf{r}) = \int_{BZ} d\mathbf{k} f_{i,p}(\mathbf{k}) e^{i\mathbf{k}\cdot\mathbf{r}} \mathbf{E}_{\mathbf{k}i}(\mathbf{r}), \quad (\text{S1})$$

where ρ is the in-plane component of \mathbf{r} , $\mathbf{E}_{\mathbf{k}i}(\mathbf{r}) e^{i\mathbf{k}\cdot\mathbf{r}}$ are the Bloch modes of the i -th band from which the heterostructure mode is

derived, and $f_{i,p}(\mathbf{k})$ is some envelope function. As mentioned in the main text, we assume further that $f_{i,p}(\mathbf{k})$ is narrowly centered around the band-edge, and so approximate $\mathbf{E}_{\mathbf{k}i}(\mathbf{r}) \approx \mathbf{E}_{\mathbf{k}_0i}(\mathbf{r})$, where \mathbf{k}_0 is the band-edge Bloch vector (M for $i = 1$ and Γ for $i = 2$). With these assumptions, the overlap integral in the numerator of eq. (1) in the main text becomes

$$\int d\mathbf{r} \epsilon_0 \bar{\chi}^{(2)} \mathbf{E}_{1,p}^* \mathbf{E}_{1,p} \mathbf{E}_{2,p'} = \int d\mathbf{r} \epsilon_0 \bar{\chi}^{(2)} \mathbf{E}_{M,1}^* \mathbf{E}_{M,1} \mathbf{E}_{\Gamma,2} \times \quad (\text{S2})$$

$$\int d\mathbf{k} d\mathbf{k}' d\mathbf{k}'' f_{1,p}^*(\mathbf{k}) f_{1,p}^*(\mathbf{k}') f_{2,p'}(\mathbf{k}'') e^{i(\mathbf{k}+\mathbf{k}'+\mathbf{k}'')\cdot\rho}, \quad (\text{S3})$$

where we have used a short-hand notation for the tensor product between the $\chi^{(2)}$ -tensor and the electric field vectors (see eq. (1) in the main text for the full expression). Since the field of a localized mode in a dielectric structure has to be real, we have $f_{1,p}(\mathbf{k}) = f_{1,p}^*(-\mathbf{k})$. We can also make some further assumptions to better understand this overlap integral. Namely, assuming that $f_{2,p}(\mathbf{k})$ is just a delta-function centered at $\mathbf{k} = 0$, and that the integral on line (S3) is dominated by the phase-matched modes $\mathbf{k} = -\mathbf{k}'$ (since we have set $\mathbf{k}'' = 0$), the (S3) integral simplifies to

$$(\text{S3}) \approx f_{2,p'}(0) \int d\mathbf{k} |f_{1,p}(\mathbf{k})|^2, \quad (\text{S4})$$

which is always nonzero. Thus, for a heterostructure design, what is most important is to ensure that the overlap of the periodic parts of the Bloch fields is non-vanishing, namely the term

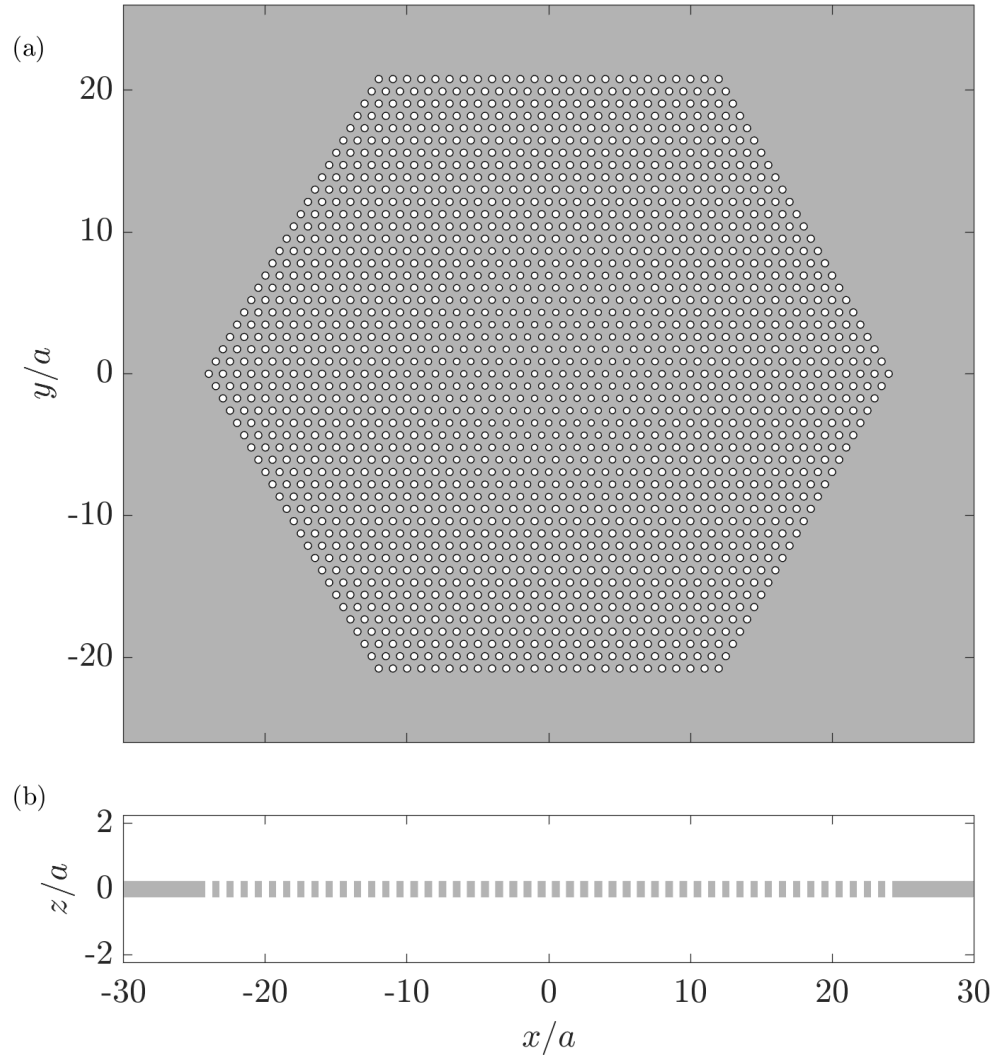


Fig. S1. Schematic of the simulated heterostructure cavity from the main text, with $(N_c, N_t, N_o) = (6, 4, 14)$ and $(r_c, r_t, r_o) = (0.22a, 0.23a, 0.25a)$; gray indicates GaN, white indicates air. (a): Cross-section at $z = 0$. (b): Cross-section at $y = 0$. The boundaries of both panels match the simulation domain boundaries, beyond which perfectly-matched layers are applied in all directions.

on line (S2), which motivates Condition 4 in the main text:

$$I = \int d\mathbf{r} \epsilon_0 \bar{\chi}^{(2)} \mathbf{E}_{M,1}^* \mathbf{E}_{M,1}^* \mathbf{E}_{\Gamma,2}. \quad (\text{S5})$$

CONVERSION EFFICIENCY

We study the conversion efficiency P_o/P_i^2 in the limit of undepleted pump, where P_i is the input power at the FH frequency, and P_o is the collected SH signal power. We label by Q_{1t}^i , Q_{2t}^i , the total quality factor of the two modes, accounting for all radiative and non-radiative losses (including emission to the input/output channel), and by Q_{1c}^i , Q_{2c}^i , the quality factor associated to the input/output channel only. Then, the efficiency can be written as [1, 2]

$$\frac{P_o}{P_i^2} = \frac{8}{\omega_1} \left(\frac{\chi_{\text{eff}}^{(2)}}{\sqrt{\epsilon_0 \lambda_1}} \right)^2 |\bar{\beta}|^2 Q_{1t}^2 Q_{2t}^2 \frac{Q_{1t}^2}{Q_{1c}^2} \frac{Q_{2t}^2}{Q_{2c}^2}, \quad (\text{S6})$$

where ϵ_0 is the permittivity of free space and $\chi_{\text{eff}}^{(2)}$ is determined by the magnitude of the relevant elements in the susceptibility tensor. In order to simulate the experimental setup of Fig. 3(f) in the main text, we assume that $Q_{1t}^{-1} = Q_{1r}^{-1} + Q_{1e}^{-1}$, where Q_{1r} is the radiative loss rate computed for the cavity mode and shown in Fig. 3(a)-(b) in the main text, and Q_{1e} is an extrinsic loss rate that could account for effects like linear absorption and disorder-induced scattering. Further, we assume that the coupling to the input/output channel is a fraction of the total far-field emission, and denote the ratio as $r_{1c} = Q_{1r}/Q_{1c}$. With the same definitions for Q_{2c} , eq. (S6) then reads:

$$\frac{P_o}{P_i^2} = \frac{8}{\omega_1} \left(\frac{\chi_{\text{eff}}^{(2)}}{\sqrt{\epsilon_0 \lambda_1}} \right)^2 |\bar{\beta}|^2 \frac{Q_{1t}^4}{Q_{1r}^2} \frac{Q_{2t}^2}{Q_{2r}^2} r_{1c}^2 r_{2c}, \quad (\text{S7})$$

Finally, we look at the maximum value of the term

$$\frac{Q_{1t}^4}{Q_{1r}^2} \frac{Q_{2t}^2}{Q_{2r}^2} r_{1c}^2 r_{2c} = \frac{(Q_{1r}^{-1} + Q_{1e}^{-1})^{-4}}{Q_{1c}^2} \frac{(Q_{2r}^{-1} + Q_{2e}^{-1})^{-2}}{Q_{2c}}, \quad (\text{S8})$$

as a function of Q_c and Q_r . Firstly, it is obvious that this is maximized when Q_{ic} is the lowest possible, which is when $Q_{ic} = Q_{ir}$, or in other words $r_{ic} = 1$ for $i = 1, 2$ (all the radiation is in the input/output channels). Next, given a fixed external loss rates Q_{1e} , the usual observation [1, 2] holds that this term is maximized as a function of Q_{ir} at the ‘‘critical’’ condition $Q_{ir} = Q_{ie}$. Now, if $Q_{ie} > Q_{ir}$, it is not possible to tune Q_{ir} to values higher than those associated to the intrinsic cavity radiation rate. However, if $Q_{ie} < Q_{ir}$, we can imagine tuning down Q_{ir} through far field engineering in order to maximize the efficiency. Thus, to obtain the results shown in Fig. 3(h) in the main text, we assumed a reduced $Q'_{1r} = Q_e$ in cases when Q_e was smaller than the intrinsic Q_{1r} . Note that for the SH mode, the Q_e values in the figure are always larger than Q_{2r} .

RESONANCE TUNING

Obviously, tuning the exact double resonance is crucial to the SHG efficiency. The wavelength of the FH mode needs to match twice the wavelength of the SH mode to within less than a nanometer, and, given unpredictable experimental fluctuations, it is important to have control over this matching. Thus, to illustrate the possibility of tuning of the FH and SH modes in

resonance, we first study the band-edge wavelength of the regular PhC bands from which the two modes are derived. Namely, in Fig. S6, we show the band-edge wavelengths as a function of the structural parameters for the PhC of Fig. 1 in the main text, which is also the PhC in the core region of the cavity studied in Figs. 2 and 3. Specifically, the starting structure has $a = 580\text{nm}$, $d = 0.28a = 162.4\text{nm}$ and $r = 0.22a = r = 127.6\text{nm}$. In Fig. S6, we explore how the band-edge wavelengths change as a function of one of these parameters, while keeping the other two fixed. In panels (a) and (b), we plot the dependence on d (a) and r (b), while in panel (c) we show the dependence vs. a for fixed (in nanometers) d and r . As can be seen, tuning any one of these structural parameters leads to a crossing of the band-edge wavelengths.

To show that this can also be used to tune the cavity modes, in Fig. S7(a) we show the dependence of the resonance wavelengths of the FH and the SH modes of a heterostructure cavity on the lattice constant a . The results are for the same cavity as in Fig. 2 of the main text, and we fix, as before, $d = 162.4\text{nm}$. Furthermore the values of the radii in the three regions are also kept the same (in nm). We see that the double-resonance condition can indeed be achieved by scanning the lattice constant. In panel (b), we show that the dependence of the radiative quality factor on a is rather weak.

REFERENCES

1. A. Rodriguez, M. Soljačić, J. D. Joannopoulos, and S. G. Johnson, ‘‘ χ (2) and χ (3) harmonic generation at a critical power in inhomogeneous doubly resonant cavities,’’ *Opt. Express* **15**, 7303–7318 (2007).
2. Z. Lin, X. Liang, M. Lončar, S. G. Johnson, and A. W. Rodriguez, ‘‘Cavity-enhanced second-harmonic generation via nonlinear-overlap optimization,’’ *Optica* **3**, 233–238 (2016).

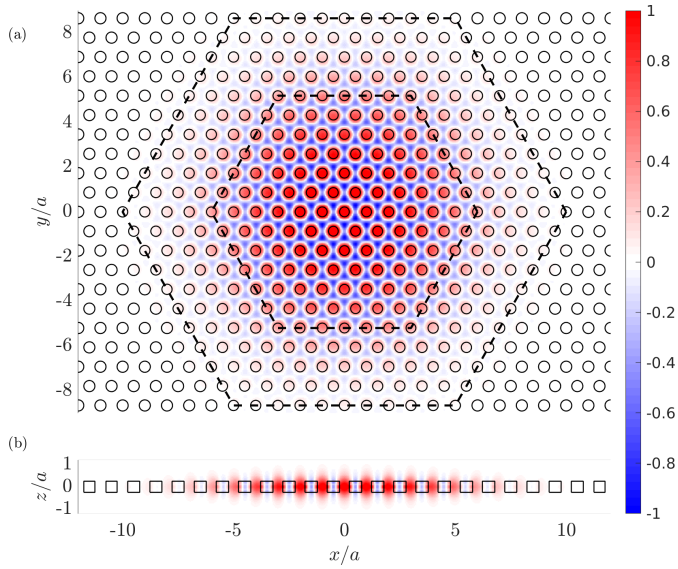


Fig. S2. Real part of the E_z profile of the ω_2 mode shown in Fig. 2(b) in the main text. (a): Cross-section at $z = 0$. Dashed hexagons show the core and the transition regions. (b): Cross-section at $y = 0$.

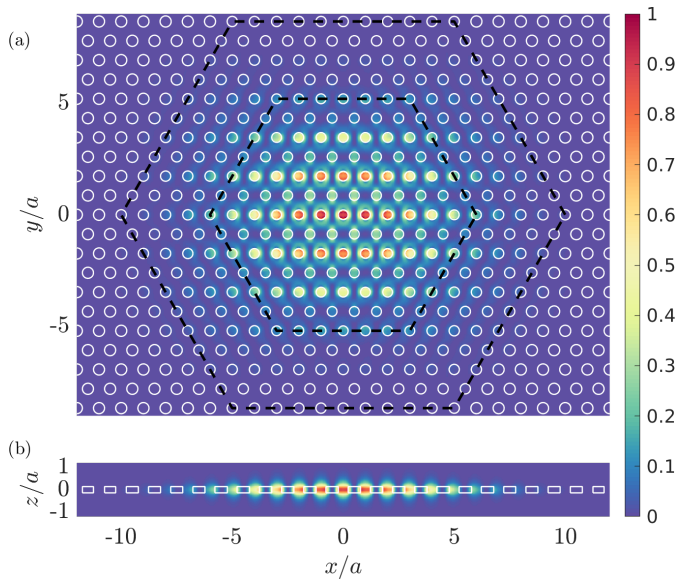


Fig. S3. Field intensity profile of the $\omega_{1,1}$ mode shown in Fig. 2(c) in the main text. (a): Cross-section at $z = 0$. Dashed hexagons show the core and the transition regions. (b): Cross-section at $y = 0$.

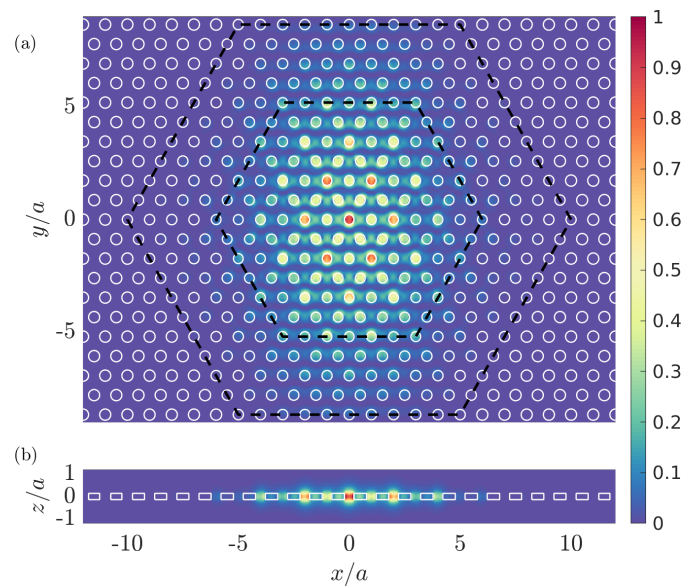


Fig. S4. Field intensity profile of the $\omega_{1,2}$ mode shown in Fig. 2(d) in the main text. (a): Cross-section at $z = 0$. Dashed hexagons show the core and the transition regions. (b): Cross-section at $y = 0$.

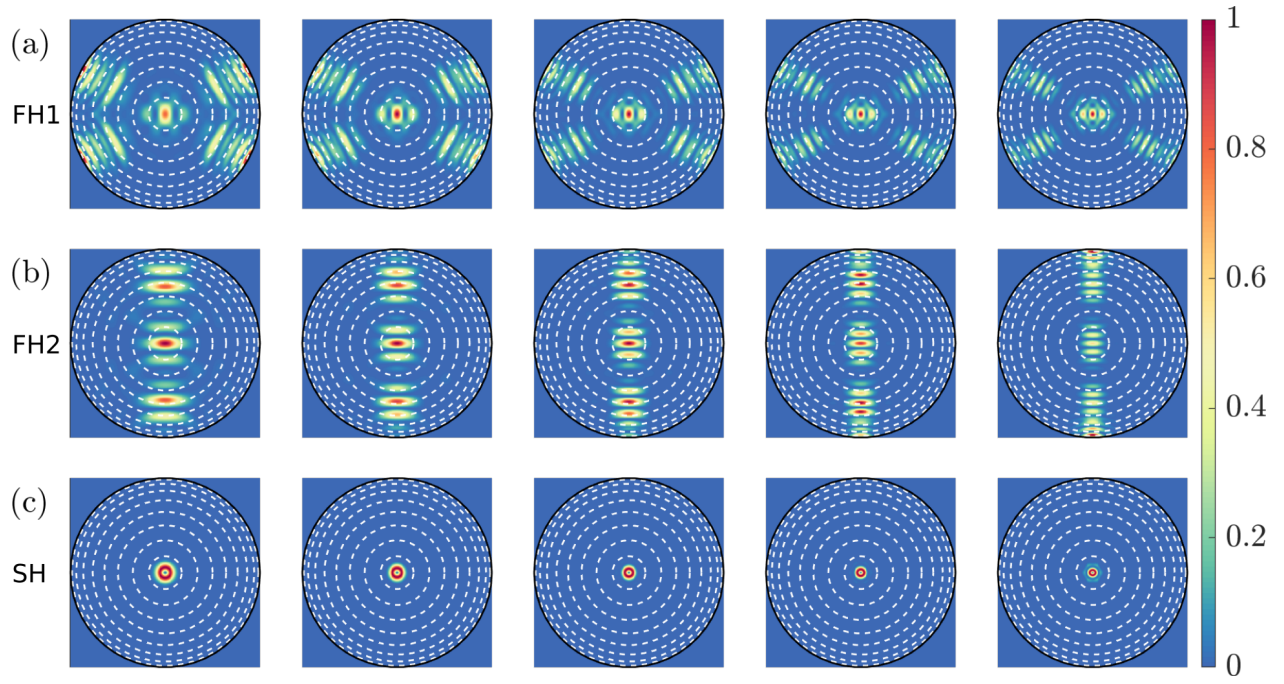


Fig. S5. Far-field profiles as in Fig. 3(c)-(d) in the main text, for $N_c = 4$ in the left-most panels to $N_c = 12$ in the right-most panels, in steps of 2. (a): For the $\omega_{1,1}$ mode; (b): for the $\omega_{1,2}$ mode, and (c): for the ω_2 mode.

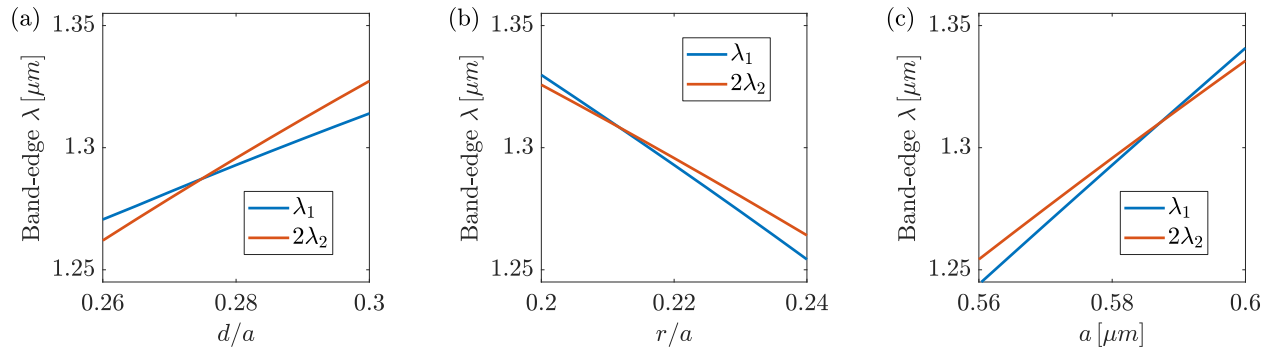


Fig. S6. For a regular PhC, band-edge wavelength of the FH band (λ_1) and twice the band-edge wavelength of the SH band ($2\lambda_2$) as a function of the PhC parameters in the vicinity of those used in the core region of the cavity from the main text, namely $d/a = 0.28$, $r/a = 0.22$, $a = 580\text{nm}$. (a): Tuning d/a ; (b): tuning r/a ; (c): tuning a , with fixed $d = 0.28 \times 580\text{nm}$ and $r = 0.22 \times 580\text{nm}$.

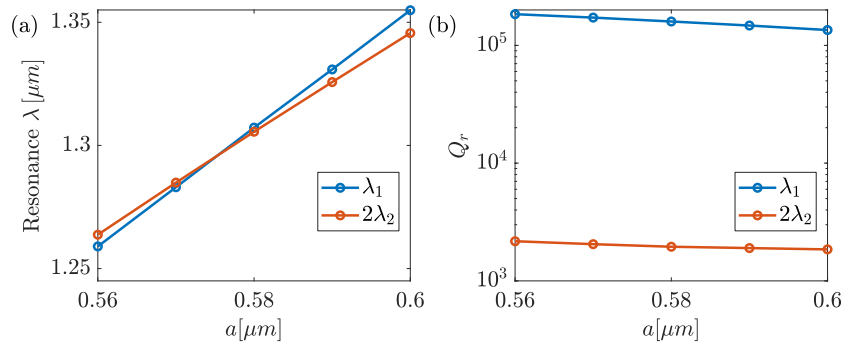


Fig. S7. (a): Resonance wavelength and (b): radiative quality factor for the two modes of the cavity shown in Fig. 2 of the main text as a function of the lattice constant a , with fixed $d = 0.28 \times 580\text{nm}$ and $r = 0.22 \times 580\text{nm}$.